https://doi.org/10.5194/egusphere-2026-3568
Preprint. Discussion started: 28 July 2026

Global MPAS-A Simulations with a Constant Pressure Upper Boundary

Joseph Klemp klemp@ucar.edu[1], Willam Skamarock [1], Soudeh Kamali [1], Han-Li Liu [1], and Jihyeon Jang [1]

[1]NSF National Center for Atmospheric Research, Boulder, Colorado, 80301, USA

Correspondence: Joseph Klemp klemp@ucar.edu (EMAIL)

Abstract. The height based vertical coordinate in the Model for Prediction Across Scales - Atmosphere (MPAS-A) was recently modified to optionally allow the upper boundary of the model domain to follow a constant pressure surface, which enables the vertical expansion and contraction of the atmosphere in response to diabatic heating and cooling for deep atmosphere applications extending into the mesosphere and thermosphere. The current study extends the testing of this generalized upper boundary formulation to assess its viability in global environments and for its use in real data applications. For a domain extending well into the thermosphere, an idealized 2-D diurnal heating test case was adapted to a 3-D global configuration and used to simulate a nearly steady periodic diurnal response that is qualitatively similar to the behavior seen in a full physics simulation with the Whole Atmosphere Community Climate Model with thermosphere and ionosphere extension (WACCM-X) at the spring equinox. For the real data test cases, the top boundary height was lowered to a nominal height of 70 km in order to initialize MPAS-A with data interpolated within the data range of IFS ERA5 analyses. Simulations on a 120 km global mesh conducted in each of the four seasons confirmed the stability of the numerical integrations and were in good qualitative agreement with the ERA5 analyses in comparisons at 10 days. The suitability of this constant pressure upper boundary formulation for higher horizontal resolution applications was also documented in simulations on a 15 km global mesh and a 60-3 km variable resolution mesh.

1 Introduction

In numerically simulating atmospheric phenomena that extend into the thermosphere, it is important to allow the atmosphere to expand/contract vertically in response to the significant diabatic heating/cooling that occurs at these high altitudes. Models that utilize the hydrostatic approximation typically use a pressure based vertical coordinate in which the upper boundary corresponds to a constant pressure surface and therefore has vertical mobility [e.g., the TGCM; Dickinson et al. (1981), and the WACCM-X; Liu et al. (2010)]. On the other hand, extensions of nonhydrostatic models into the thermosphere have been implemented with height based vertical coordinates [e.g. the GITM; Ridley et al. (2006), the ENDGame Model; Griffith et al. (2020), the UA-ICON Model; Borchert et al. (2019), MPAS-A; Klemp and Skamarock (2021), and NEPTUNE; Kelly et al. (2023)], for which a rigid lid that does not allow vertical expansion/contraction of the model domain is the natural upper boundary condition. To relax this constraint, Ridley et al. (2006) specified zero vertical gradients in vertical fluxes to remove the rigid

https://doi.org/10.5194/egusphere-2026-3568
Preprint. Discussion started: 28 July 2026

lid and Kelly et al. (2023) derived boundary conditions that permit mass flux through the boundary in response to internal heating/cooling within vertical columns. Following a different approach, Klemp and Skamarock (2022, hereafter KS22) developed a modification to the height-based vertical coordinate that allows the coordinate surfaces to adaptively follow a constant pressure surface at the top of the model domain. This formulation requires only minor changes to the model code and maintains the benefits of stationary hybrid terrain-following coordinate surfaces throughout the troposphere while permitting a constant pressure boundary condition along the top surface of the model domain. It not only allows vertical expansion/contraction of the model domain, but also maintains exact conservation of scalar mass since the top boundary remains a material surface. KS22 demonstrated the viability of this upper boundary formulation in simulations of an idealized 2-D diurnal heating test case for a deep atmosphere extending well into the thermosphere, and documented the potentially large artificial behavior that can arise if a rigid-lid upper boundary is imposed instead.

In this paper, we conduct further testing to examine the suitability of employing the KS22 constant pressure upper boundary formulation in more general global applications. We begin in section 2 by extending the 2-D idealized diurnal heating test case described in KS22 to a 3-D global environment. With this added complexity, although we no longer have a linear analytic solution for comparison, we can get qualitative guidance from a representative simulation obtained with the WACCM-X Model (Liu et al., 2018). This is a new idealized thermospheric test case with highly simplified physics that may also prove useful to others in evaluating the behavior of their model dynamics in the thermosphere. In section 3, we then examine its application in real-data simulations for model configurations that are consistent with model tops in current operational global numerical weather prediction (NWP) models, such as the German ICON Model with a 75 km top (Müller et al., 2025) and the UK Met Office EndGame Model at 85 km (Willett et al., 2026). For NWP applications, the objective is typically to place the upper boundary above the levels of primary meteorological interest in the troposphere. The mesospheric levels at which NWP model tops are placed are also driven by the need to assimilate satellite radiances, which have attenuation profiles that extend into the mesosphere. Since both a rigid lid and a constant pressure upper boundary are totally reflective to upward propagating gravity wave energy, an absorbing layer is generally implemented below the upper boundary to mitigate these artificial reflections. Thus, either a rigid lid or a constant pressure upper boundary may be suitable (Pu and Kalnay, 2018) for NWP applications. To evaluate the viability of the KS22 upper boundary for real-data NWP simulations, we conduct tests in different seasons and at different horizontal resolutions for global domains with the top boundary at a nominal height of 70 km. Here, we have IFS analyses for comparison, although we recognize that the model physics in MPAS-A and the IFS differ significantly, and that the MPAS-A physics have not yet been specifically adapted for these greater domain heights. Thus, these comparisons are more for assessing the behavior of the upper boundary implementation than for evaluating the absolute accuracy of the simulations. Through comparative simulations with a rigid lid upper boundary, we also confirm that choosing either a constant pressure or a rigid lid upper boundary produces comparable results for these NWP test cases.

As part of the NSF NCAR initiative to develop the System for Integrated Modeling of the Atmosphere (SIMA), MPAS-A has been adapted as one of the dynamical cores for the Whole Atmosphere Community Climate Model (WACCM) (Kamalli et al., 2024). This constant pressure upper boundary will make it possible for further development of MPAS-A as a dynamical core

https://doi.org/10.5194/egusphere-2026-3568
Preprint. Discussion started: 28 July 2026

for WACCM with thermosphere and ionosphere extension (WACCM-X), which will provide a further step toward achieving the desired deep atmosphere nonhydrostatic modeling system.

2 Diurnal heating test case

The 2-D diurnal heating test case described in KS22 is based on a linear analytic solution for a steady periodic wave driven by a propagating internal heating function. To modify this test case for a global domain, we specify an initial temperature field and a time dependent diurnal heating rate that are essentially the same as that in KS22 at the equator, but that taper the initial temperature perturbation and the heating rate to zero at the north and south poles. Thus, the initial temperature T_{t_0} at the constant pressure upper boundary is defined to be

$$T_{t_0} = \overline{T} + \Delta T_d \cdot \sin\lambda \cos\gamma, \tag{1}$$

where $\overline{T}$ is the initial mean temperature at the top boundary, and ΔT_d defines the amplitude of the initial sinusoidal diurnal variation along this upper boundary. In specifying the horizontal variation of T_{t_0}, γ and λ denote the latitude and longitude, respectively. The initial temperature field is specified in a form that permits the hydrostatic equation to be integrated vertically to yield a closed form analytic expression for pressure. For this implementation on the globe, the initial temperature maintains the same form as in the 2-D case, given in KS22 (14):

$$T_L = T_t \left[\frac{T_t}{T_b}(1 - \tanh\tilde{z}) + \tanh\tilde{z} \right]^{-1}. \tag{2}$$

Here, T_L is the temperature from the analytic solution as described in KS22, T_t is the temperature at the constant pressure upper boundary, T_b is the constant temperature at the fixed height z_b of the lower boundary of the simulation domain, and z_d is the scale height for the lower level vertical temperature gradients, with $\tilde{z} = (z - z_b)/z_d$.

As mentioned above, we seek qualitative guidance in evaluating the results from this idealized test case through comparisons with a simulation from the WACCM-X model (Liu et al., 2018). For this purpose, we have chosen a WACCM-X simulation valid at 00Z on 21 March 2000 because at the spring equinox the global flow fields are most symmetrical about the equator, based on climatology. Following KS22, we place the lower boundary at $z_b = 100$ km, where we specify a constant temperature $T_b = 200$ K and pressure $p_b = 0.03$ Pa, consistent with the conditions at 100 km in the WACCM-X simulation. At the top boundary of the simulation domain, we specify an initial mean height $H_0 = 600$ km, and define the initial top temperature T_{t_0} from (1) using $\overline{T} = 850$ K and $\Delta T_d = 150$ K for this test case. These parameters are the same as those used in KS22 except that $\overline{T}$ has a lower value for better consistency with this WACCM-X simulation.

To achieve a constant pressure upper boundary condition in MPAS, KS22 implemented a coordinate transformation in the upper portion of the model domain to allow the coordinate surfaces to transition adaptively from a constant height surface at a specified height z_p to one at height H that follows a specified constant pressure surface at the model top:

$$z = \left(\frac{\zeta - z_p}{H_0 - z_p} \right)^2 (H - H_0) + \zeta, \quad \text{for} \quad z > z_p \tag{3}$$

https://doi.org/10.5194/egusphere-2026-3568
Preprint. Discussion started: 28 July 2026

such that the transformed coordinate $\zeta = H_0$ at $z = H$. For this test case, we follow KS22 and set $z_p = 200$ km. We specify the desired constant pressure along the top boundary to be $p_{top} = 2.18\text{x}10^{-8}$ Pa, which is the value obtained by vertically integrating the sounding with $T_t = \overline{T}$ in (2) from z_b to H_0. We then adjust the height H of the top boundary at the end of each time step based on the deviations of the top pressure from the target value p_{top} using the hydrostatic vertical extrapolation based on $\phi = \ln(p/p_0)$ as defined in KS22 eq. (5):

$$H = H^* + \alpha \frac{R_d T^*}{g}(\phi^* - \phi_{top}), \tag{4}$$

where the asterisk superscript denotes values along the upper surface at the current time step or iteration and $\phi_{top} = \ln(p_{top}/p_0)$. The dimensionless height adjustment coefficient α is unity for a full hydrostatic extrapolation, but can be adjusted to smaller values to remove any oscillations in the upper boundary height, if necessary.

We initialize the thermodynamic fields and the height of the constant pressure upper boundary by utilizing the iterative technique described in KS22. With this approach, we first compute the hydrostatically balanced thermodynamic fields using (2) and (1) based on a rigid-lid upper boundary at the nominal height of the top boundary H_0.The height adjustment coefficient α is set at its full value $\alpha = 1.0$ for this test case. With the new height H, we reinitialize the thermodynamic fields on the modified coordinate surfaces and continue the iterative process. This approach yields a well converged initialization with a constant pressure along the model upper boundary in three iterations. The initial temperature field is displayed in the vertical cross section along the equator in Fig. 1, which is similar to Fig. 2 in KS22.

The diurnal heating rate Q_d governs the evolution of the flow as a forcing term in the thermodynamic equation. Taking the time derivative of (2), Q_d becomes

$$Q_d = \frac{\partial T_L}{\partial t} = \frac{\partial T_t}{\partial t} \tanh \tilde{z} \left[\frac{T_t}{T_b} + \left(1 - \frac{T_t}{T_b}\right) \tanh \tilde{z} \right]^{-2}. \tag{5}$$

Here, (5) is the same as in KS22 except that the second term in the numerator of KS22 (15) has been dropped as it is negligible for this case. In defining this heating rate, we specify that the temperature at the model top T_t maintains the same form as in (1) but includes a diurnal propagation:

$$T_t = \overline{T} + \Delta T_d \cdot \sin(\lambda + 2\pi\omega t) \cos\gamma, \tag{6}$$

where $\omega = \text{day}^{-1}$, and thus

$$\frac{\partial T_t}{\partial t} = 2\pi\omega \Delta T_d \cdot \cos(\lambda + 2\pi\omega t) \cos\gamma. \tag{7}$$

In simulating this test case on the globe, we employ the same configuration of MPAS-A as in the 2-D simulations described in KS22 except that the 2-D mesh configuration is replaced by the 10242 cell global mesh (~240 km horizontal grid size). We employ the transformed vertical coordinate described in KS22 that follows the height of the time dependent constant pressure upper boundary as described in KS22 with a constant $\Delta\zeta = 5$ km nominal vertical grid spacing on the transformed grid.

After initializing the model fields as described above, the dynamical equations are stepped forward in time using the split-explicit integration numerics in MPAS-A, as described in Skamarock et al. (2012), with an overall time step of $\Delta t = 600$ s and

https://doi.org/10.5194/egusphere-2026-3568
Preprint. Discussion started: 28 July 2026

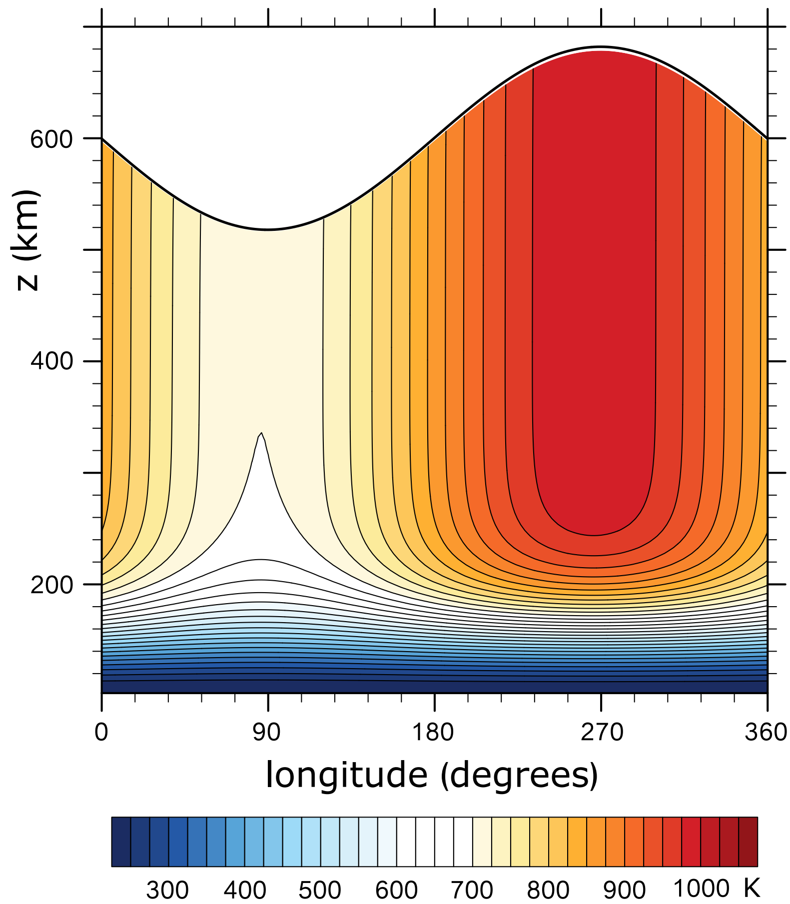

Figure 1. Initial temperature field along the equator from (2) and (1) for the idealized global diurnal heating test case.

a smaller acoustic time step $\Delta\tau = 100$ s. A diurnal heating function based on (5) and (7) is included in the prognostic equation for the potential temperature to provide the periodic thermodynamic forcing. As explained in KS22, in lieu of realistic model physics, a dissipation mechanism is required to limit the unrealistic growth of the horizontal velocity and to produce a proper phase relationship between the temperature and the zonal wind. Thus, we include a Rayleigh damping term in the horizontal velocity equation with a coefficient of $K = 0.001$ s^{-1}.

In conducting initial simulations over several diurnal periods with the above described configuration, we found that the longitudinal and meridional winds develop an essentially steady periodic structure, but the temperature field at upper levels continues to increase over time. This temperature rise appears to be associated with a net positive change in the internal energy as the simulation evolves, and may occur because appropriate cooling mechanisms, such as molecular thermal conduction, are not considered in the model. The heating function (5) we derived in KS22 for the 2-D diurnal heating case was based on the linear equations in which the horizontal winds are neglected as they are higher order. Thus, to restrict the continuing increase

https://doi.org/10.5194/egusphere-2026-3568
Preprint. Discussion started: 28 July 2026

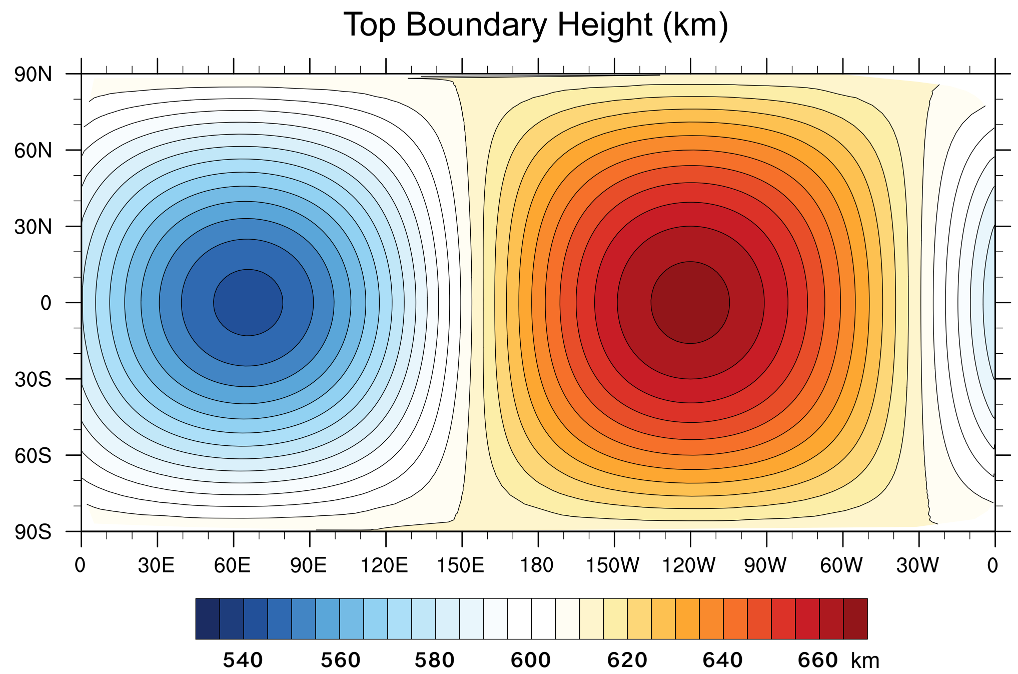

Figure 2. Height of the top boundary of the simulation domain at four days for the idealized global diurnal heating test case.

in temperature, we have modified the heating function by adding a Newtonian cooling term that acts on the deviation of the temperature from what it would be if the solution was linear and the horizontal winds were ignored. The modified heating rate then can be written as:

$$Q'_d = \frac{\partial T_L}{\partial t} - \beta(T - T_L) \quad (8)$$

where $\partial T_L/\partial t$ is as defined in (5) and T_L is the temperature based on (2) and (7). The Rayleigh damping coefficient is set at $\beta = 2 \times 10^{-5}$ s^{-1} as this was about the smallest value that still allowed the simulated temperature field to converge to a nearly steady periodic structure. Applying the adjustment (4) to the height of the upper boundary every time step, this surface maintains its initial structure as it propagates in response to the diurnal heating function (8), as illustrated in Fig. 2, which displays the top boundary height at 4 days.

The vertical cross sections of temperature and zonal velocity along the equator at four days are displayed in Fig. 3a,c. Here the temperature field exhibits some variation from its initial structure shown in Fig. 1. Although the linear analytic solution in the absence of the horizontal wind reproduces the initial state after each diurnal period, given the significant zonal winds and nonlinear effects in the global configuration, these results do not seem unreasonable. They also have good qualitative similarity to the WACCM-X fields at the spring equinox shown in Fig. 3b,d. Notice that the phase of the zonal wind propagation lags (to the east of) the phase of the temperature by about 90 degrees in the MPAS-A simulation, which is similar to the behavior seen in the WACCM-X fields.

https://doi.org/10.5194/egusphere-2026-3568
Preprint. Discussion started: 28 July 2026

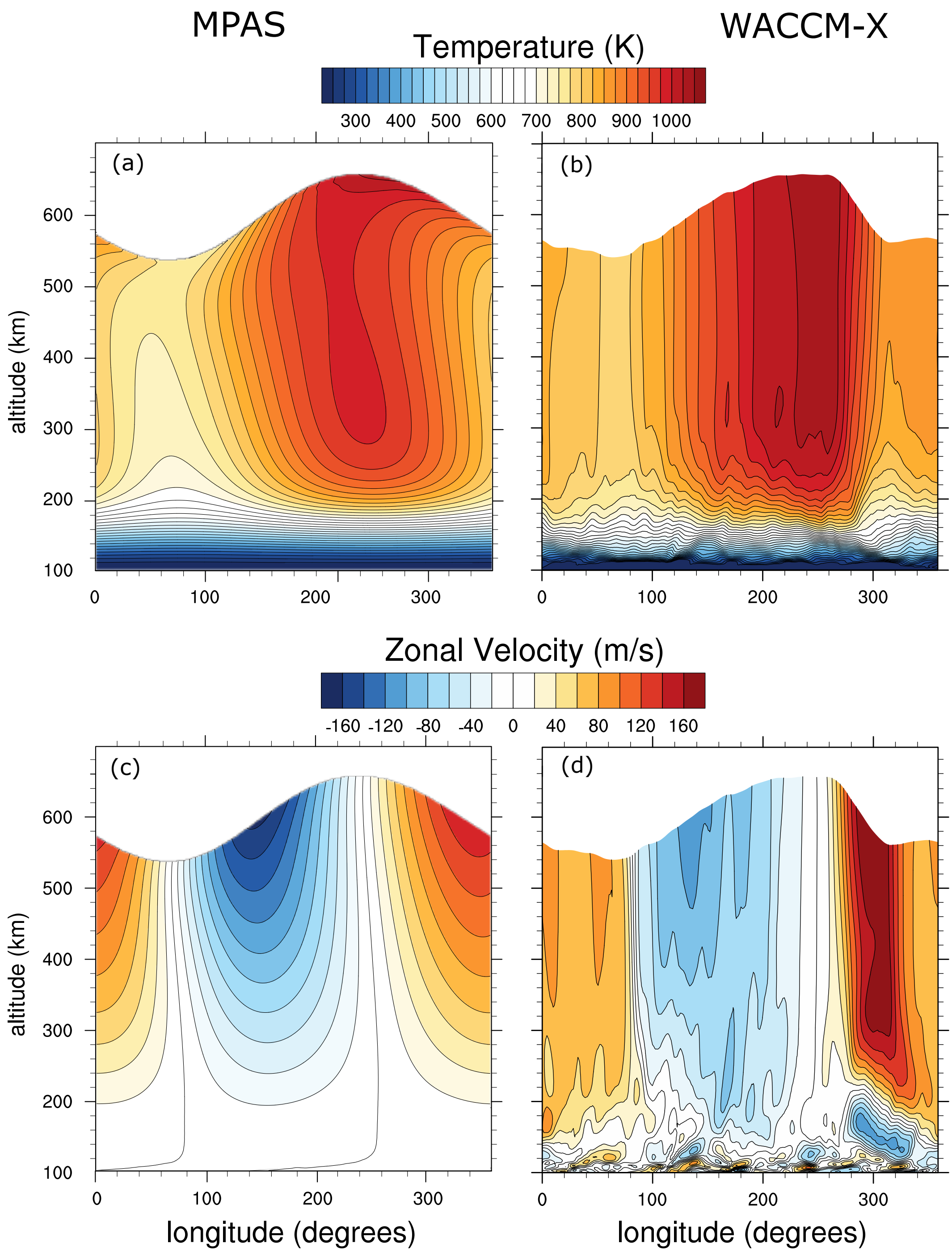

Figure 3. Vertical cross sections along the equator for temperature and zonal velocity from (a), (c) the MPAS-A simulation at four days and (b),(d) WACCM-X 2.0 Model at 0000 UTC 21 March 2000.

https://doi.org/10.5194/egusphere-2026-3568
Preprint. Discussion started: 28 July 2026

The corresponding horizontal cross sections taken along the upper model boundary for temperature, zonal velocity, and meridional velocity from the MPAS-A simulation and the WACCM-X Model are displayed in Fig. 4. Again there are qualitative similarities between the MPAS-A and WACCM-X results. The temperature fields exhibit a broad wave number one structure in the longitudinal direction with maximum perturbations along the equator. The zonal velocities display good longitudinal coherence with WACCM-X, although MPAS-A does not capture the more localized velocity extremes in WACCM-X near the poles. Both MPAS-A and WACCM-X exhibit strong meridional velocities over the poles with weak flow in the vicinity of the equator. Notice that the MPAS-A cross sections in Fig. 4a,c,e do not include the continental boundaries as shown in Fig. 4b,d,f for WACCM-X. This is because the lower boundary in our idealized MPAS-A simulations is at a fixed height that does not include any terrain effects.

While we can't verify the quantitative accuracy of this global diurnal heating simulation with a constant pressure upper boundary, we can confirm that the evolving simulation maintains a structure along the equator (Fig. 3a,c) that is very similar to the 2-D diurnal heating test case in KS22 and that the overall global structure is qualitatively similar to that exhibited in a full physics WACCM-X simulation at the Spring solstice (Figs. 3,4). Importantly, the numerics associated with this upper boundary formulation appear to be robust, without the appearance of any small scale noise or instability.

For this test case, removing the rigid lid constraint with the KS22 constant pressure upper boundary is critically important. For the 2-D diurnal heating test case, KS22 demonstrated that with the rigid lid boundary condition, artificial temperature perturbations form just beneath the upper boundary that are so large that they can actually drive the temperature locally negative and produce numerical instability. The global diurnal test case with a rigid lid configuration produces this same artificial behavior and is therefore not an option for comparison purposes.

3 Real data simulations

To evaluate the behavior of the constant pressure upper boundary condition proposed by KS22 in real data applications, we have conducted global simulations with full physics MPAS-A configurations in each of the four seasons (April, July, and October in 2018 and January in 2019). We begin with a 40962 cell horizontal mesh (∼120 km spacing) and configure 80 levels in the vertical with the nominal height of the top boundary set at $H_0 = 70$ km. As mentioned above, this top boundary height is comparable to other high top NWP models, and allows us to initialize from IFS ERA5 analyses. The hybrid smoothed terrain following coordinate (Klemp, 2011) is applied between the surface and 25 km, and the transition of coordinate surfaces toward a constant pressure top begins at $z_p = 25$ km. The model physics are specified using the MPAS-A mesoscale reference suite, which is appropriate for mesoscale resolutions with parameterized convection. The individual physics packages in the reference suite are listed in Table 1. We recognize that these physics representations are designed for weather simulations that focus on the troposphere/stratosphere, and may have some deficiencies at upper levels in applications extending into the mesosphere. However, we believe these physics are sufficient for our purposes in testing the viability of the proposed constant pressure upper boundary.

https://doi.org/10.5194/egusphere-2026-3568
Preprint. Discussion started: 28 July 2026

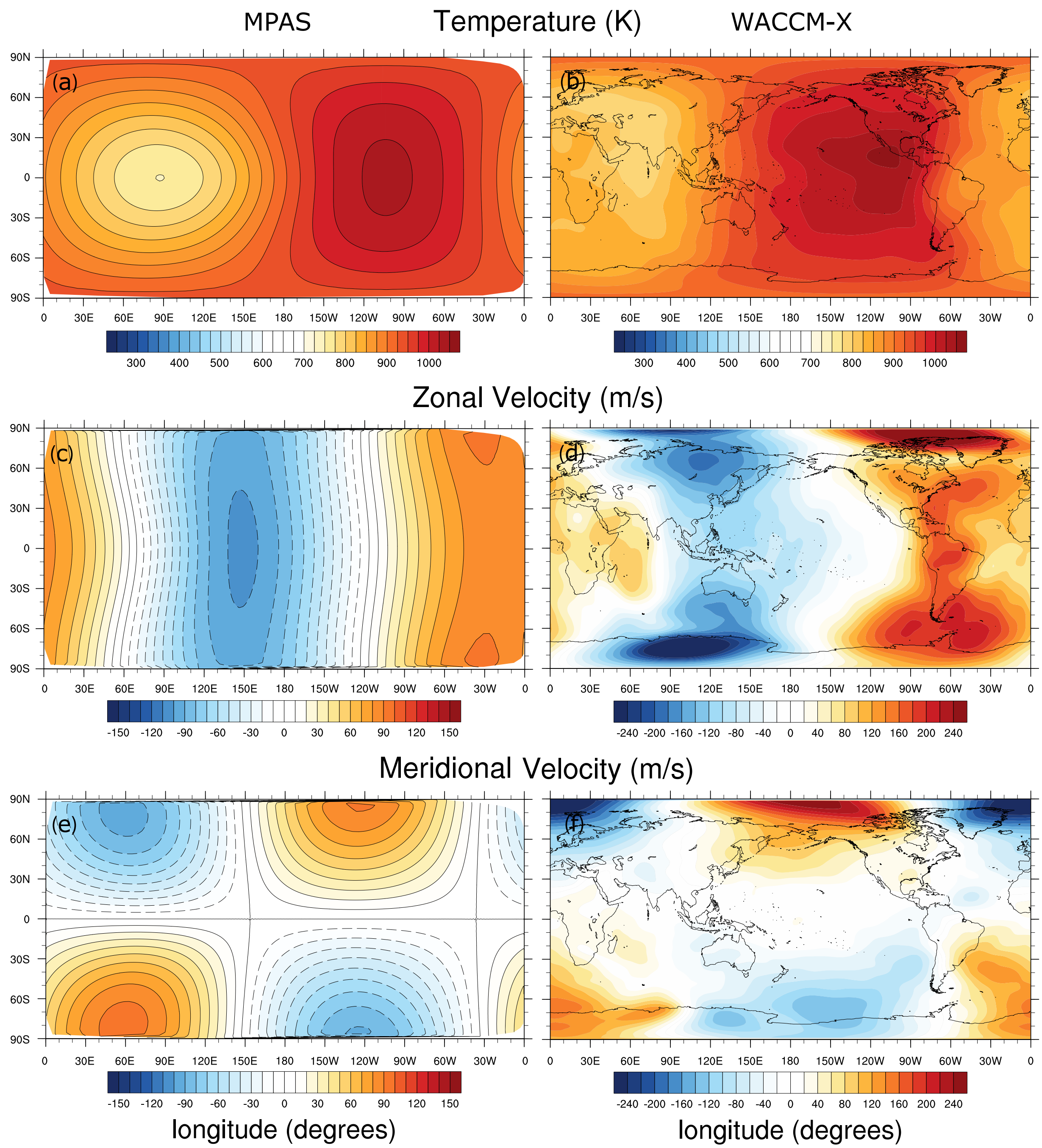

Figure 4. Horizontal cross sections at the upper model boundary for temperature, zonal velocity, and meridional velocity from (a),(c),(e) the MPAS-A simulation at four days and from (b),(d),(f) the WACCM-X 2.0 Model at 0000 UTC 21 March 2000.

https://doi.org/10.5194/egusphere-2026-3568
Preprint. Discussion started: 28 July 2026

Table 1. The set of parameterization schemes used by the 'mesoscale_reference' physics suite in MPAS-A. Further information on these physics packages can be found in Skamarock et al. (2019).

Parameterization	Scheme
Convection	New Tiedtke (WRF 3.8.1)
Microphysics	WSM6 6-class (WRF 4.5)
Land surface	Noah (WRF 4.5)
Boundary layer	YSU (WRF 4.5)
Surface layer	Revised Monin-Obukhov (WRF 4.5)
Radiation, LW	RRTMG (WRF 3.8.1)
Radiation, SW	RRTMG (WRF 3.8.1)
Cloud fraction for radiation	Xu-Randall (1996)
Gravity wave drag by orography	YSU (WRF 4.5)

The initialization for these cases follows the same iterative procedure as described for the idealized case in the previous section, except that after each iteration the thermodynamic fields are interpolated to the modified MPAS-A coordinate surfaces from the appropriate model level ERA5 reanalysis data (Hersbach et al., 2020). Beginning with a rigid lid at $H_0 = 70$ km in the first iteration, good convergence to a constant pressure surface is again achieved in three iterations. We specified the target pressure p_{top} such that the maximum and minimum heights of the initial upper pressure surface were centered above and below the nominal 70 km height in the initialization based on the ERA5 data for the April 2018 case. This produced the value $p_{top} = 3.884$ Pa, which was then used as the top pressure for all of the simulations.

The MPAS-A 120 km simulations were conducted with the overall time step $\Delta t = 600$ s for the physics and scalar transport, a dynamics timestep of 200 seconds, and an acoustic time step $\Delta\tau = 50$ s. During the time integration, we applied the hydrostatic height adjustment for H after every dynamics time step to allow the upper boundary to follow the target constant pressure surface as proposed in KS22. Using the full adjustment coefficient $\alpha = 1$ in (4), we found occasional instabilities arose in the simulations and therefore specified a reduced $\alpha = 0.2$ for these real data simulations. Even with this conservative value of α we found that the heights of the top boundary were nearly indistinguishable from the heights obtained in cases that were stable with $\alpha = 1$. We also employed 10 applications of the Laplacian smoother to the model top height at each adjustment step, as described by KS22, to control any small scale noise that might arise in the top boundary coordinate surface. Simulations for each of the four months were initialized at 00 UTC on the 14th day of the month, and were conducted out to 30 days to ensure that the numerical integrations maintained stability and did not create noticeable small-scale noise that would require additional filtering. To illustrate the behavior of these simulations, we display in Fig. 5a,b latitude vs altitude cross sections at zero degrees longitude for temperature and zonal velocity from simulation day 10 in the July simulation, valid at 00 UTC 24 July 2018. This period corresponds to the Antarctica winter and exhibits a strong Antarctic polar jet (maximum ~ 200 ms^{-1}) together with significantly lower temperatures over the south pole.

https://doi.org/10.5194/egusphere-2026-3568
Preprint. Discussion started: 28 July 2026

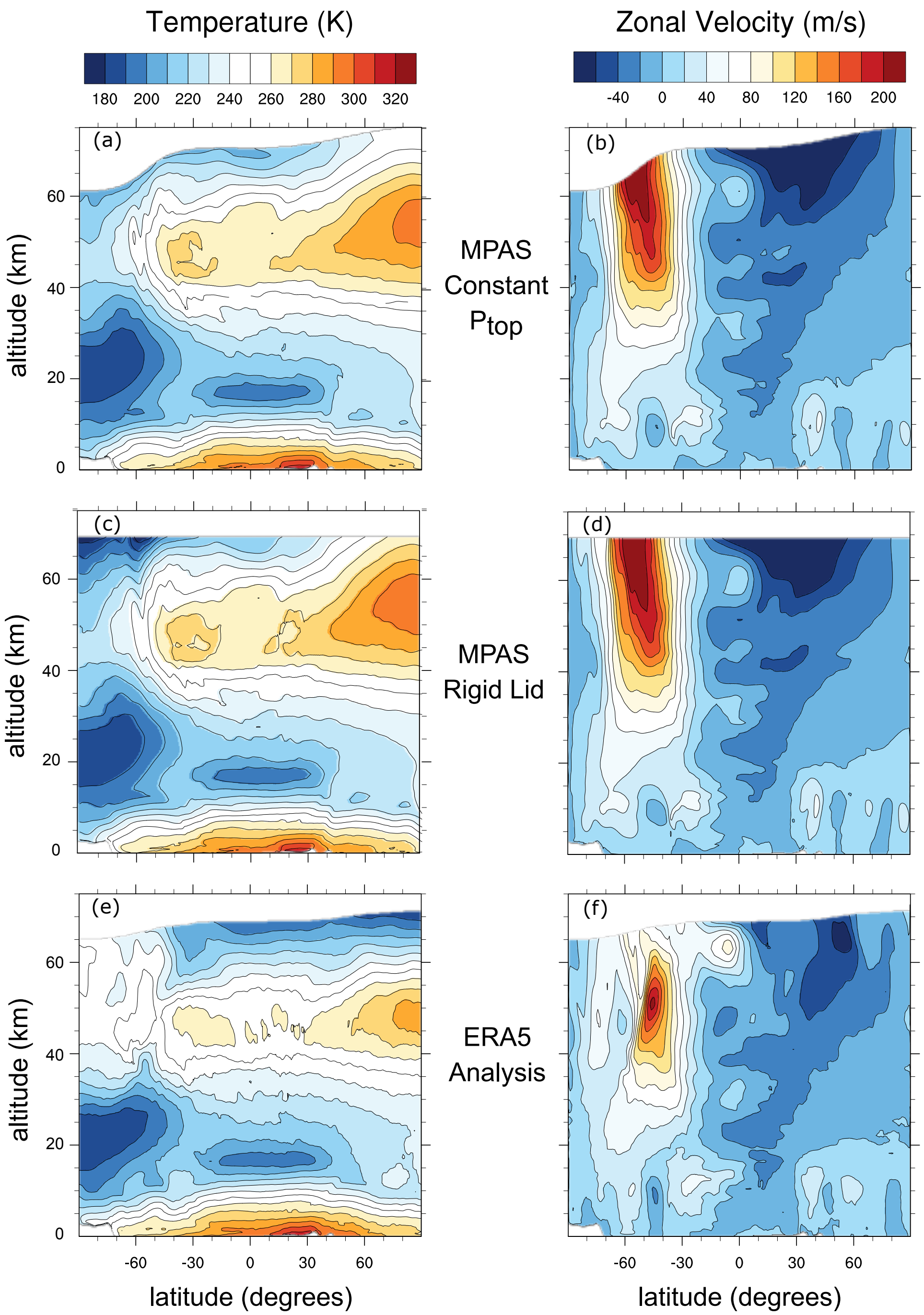

Figure 5. Latitude vs altitude cross sections of temperature and zonal velocity at zero degrees longitude for a 10 day MPAS-A forecast valid 24 July 2018 with a constant pressure upper boundary (a,b) and with a rigid-lid upper boundary (c,d). The ERA5 analysis is also displayed on this date (e,f).

https://doi.org/10.5194/egusphere-2026-3568
Preprint. Discussion started: 28 July 2026

The corresponding temperature and zonal velocity cross sections from the ERA5 analysis at this same time are depicted in Fig. 5e,f. These fields are similar to those from the MPAS-A simulation in Fig. 5a,b, although the south polar temperatures are noticeably colder and the Arctic polar jet is stronger in the MPAS-A simulation than in the ERA5 analysis. As a result, the lowering of the constant pressure boundary (evident by the top surface of the plotted data) is more pronounced in the MPAS-A simulations. We believe that these departures are most likely the result of differences in the model physics in the lower mesosphere. For example, the Yonsei University (YSU) gravity wave drag in the mesoscale reference suite is forced only by orography and does not include the sub-grid scale effects of moist convection or fronts and jets. Also ozone, which plays an important role in temperature regulation and radiative heating in the mesosphere, is specified with its climatological values rather than being prognosed.

For comparison purposes, we also simulated these cases over the four seasons with a rigid lid upper boundary in MPAS-A. Fig. 5c,d depicts the temperature and zonal wind fields for this same 10 day July simulation and exhibits very close agreement with the constant p_{top} results in Fig. 5a,b. This agreement is typical of the comparisons for simulations in the other three seasons, and appears to confirm that discrepancies between the MPAS-A simulations and the ERA5 analyses are not caused by our implementation of the constant pressure upper boundary condition. It also suggests that for simulations with a domain height at around 70 km, the constant pressure and rigid lid upper boundaries may be expected to produce comparable results more generally.

To further assess the behavior of the upper boundary that follows a constant pressure surface, we have plotted the horizontal cross sections of the top boundary height at simulation day 10 for each of the MPAS-A simulations conducted in April, July, October, and January in Fig. 6a,c,e,g, along with the height fields from the corresponding ERA5 analyses in Fig. 6b,d,f,h. Here, we see the mirror image north-south behavior between the spring and fall simulations and also between the summer and winter simulations, which is to be expected. The structure of height variations in the MPAS-A simulations is similar to that of the corresponding ERA5 analysis, although the amplitude of the variations are about a factor of two larger in the MPAS-A results. As discussed above, we believe that these differences are likely due to differences in the model physics and dissipation at upper model levels in the mesosphere.

We have also conducted additional testing to confirm that this upper boundary representation is suitable for higher resolution applications. For this purpose, we produced the 10 day global simulations for the case initialized on 14 July 2018 on the MPAS-A 2621442 cell mesh (∼15 km horizontal cell spacing). The overall time step was set at $\Delta t = 90$ s for the first eight days and then lowered to 60 s for the final two days due to the strong (~ 200 ms^{-1}) zonal winds in the south polar jet. The global solution for day 10 is very similar to that obtained in the 120 km simulation as displayed in Fig. 5.

To show some of the finer scale structure, we focus on a region over the southern Andes mountains in South America and the Antarctic Peninsula in Antarctica, where significant orographically induced waves are present in the strong south polar jet in the mesosphere. Fig. 7a displays the height of the top surface of the model domain, in which the waves in the lee of the southern tip of South America are clearly evident. The upper boundary condition we have applied in these simulations is designed to closely follow a constant pressure upper boundary surface by continuously nudging that surface toward a target constant pressure. Since smaller scale waves near the upper boundary may provide larger deviations from the desired top

https://doi.org/10.5194/egusphere-2026-3568
Preprint. Discussion started: 28 July 2026

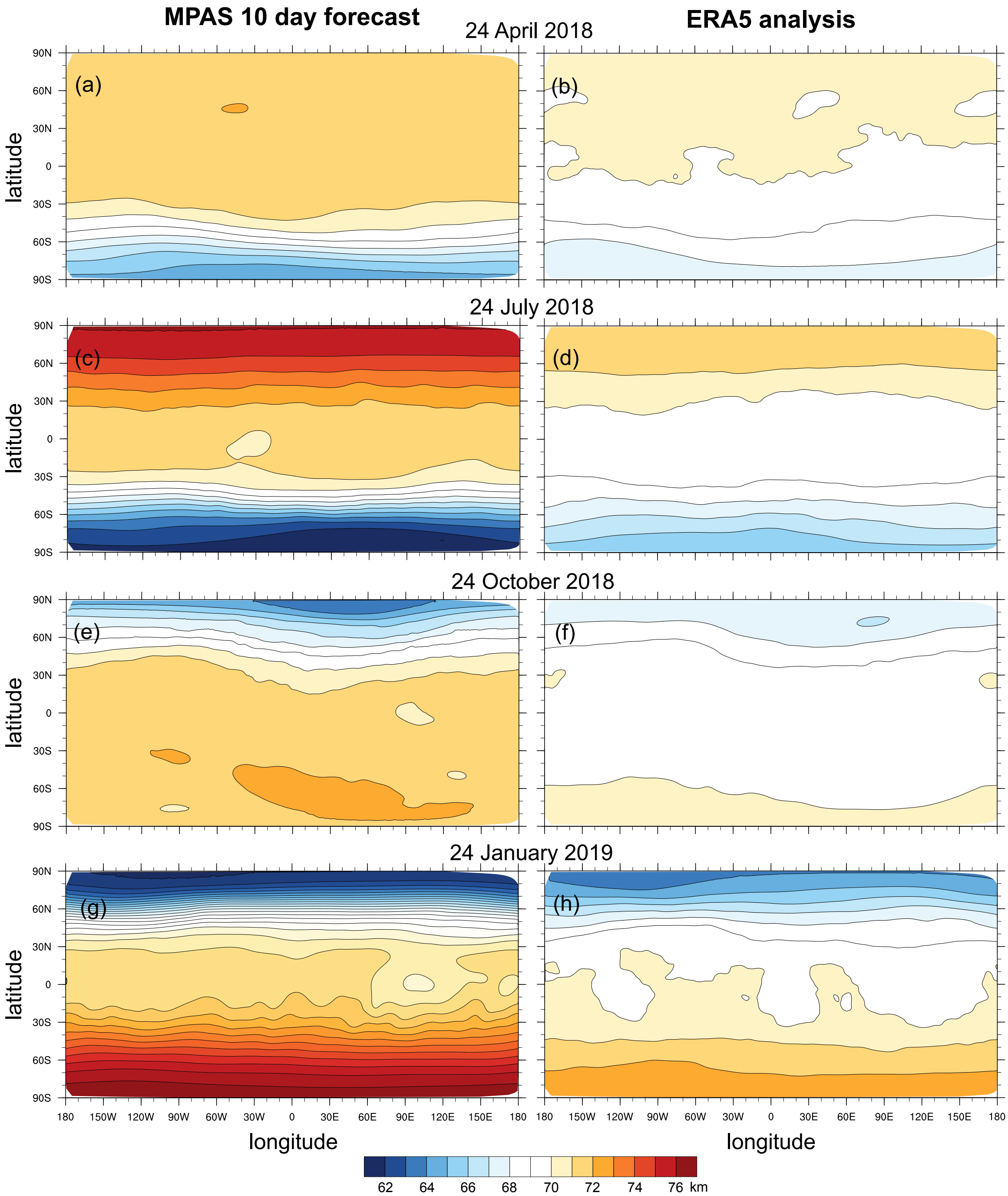

Figure 6. Horizontal cross sections of the height of the constant pressure upper boundary for 10 day MPAS-A forecasts valid at (a) 24 April 2018, (c) 24 July 2018, (e) 24 October 2018, and (g) 24 January 2019. The corresponding heights of the constant pressure p_{top} surface in the corresponding ERA5 analyses are in panels (b, d, f, and h), respectively.

https://doi.org/10.5194/egusphere-2026-3568
Preprint. Discussion started: 28 July 2026

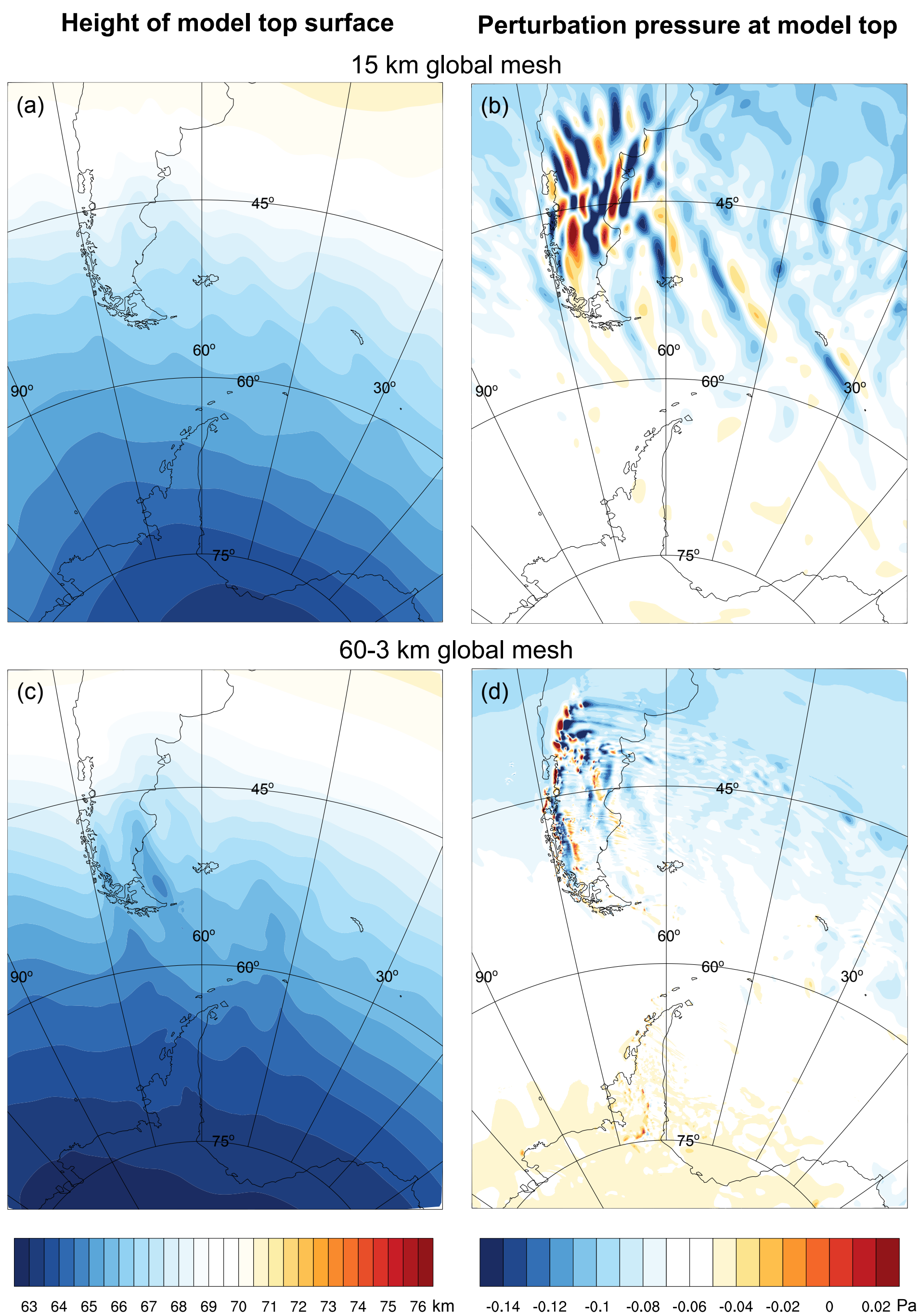

Figure 7. Horizontal cross sections of (a,c) the height of the constant pressure upper boundary and (b,d) the perturbation pressure from the target p_{top} at the model top for 10 day MPAS-A forecasts valid at 24 January 2019 for (a,b) the 15 km global mesh and (c,d) the 60-3 variable-resolution global mesh.

https://doi.org/10.5194/egusphere-2026-3568
Preprint. Discussion started: 28 July 2026

boundary pressure, in Fig. 7b we have also plotted the perturbations in the pressure along the top boundary from the specified target value $p_{top} = 3.884$ Pa. Although the wavelike structure of the pressure perturbations appears along the top surface in the lee of the Southern Andes, this surface appears well resolved and the maximum deviations from the target pressure are only a few percent of its target value of 3.884 Pa.

For a final resolution test, we have simulated this same 10 day July period using the MPAS-A 60-3 km variable-resolution mesh (mesh x20.835586) with the 3 km mesh region centered over the same region as shown in Fig. 7. This simulation was conducted using an overall MPAS-A time step of $\Delta t = 20$ s that was lowered to 15 s after eight simulation days as explained for the 15 km simulation. The heights of the upper surface at 10 days are shown in Fig. 7c and are similar to the heights in the 15 km simulation in Fig. 7a, except that additional small-scale structure is apparent due to the finer resolution of the 3 km mesh. The pressure perturbations along the top surface, shown in Fig. 7d, are noticeably smaller in amplitude than those shown in the 15 km simulation in Fig. 7b. We believe that this occurs because the waves near the upper boundary are better resolved with the 3 km mesh and therefore the height of the top surface can more accurately track the target constant pressure surface. Although there may be some nonhydrostatic contributions to the pressure near the top boundary on this 3 km horizontal mesh, the hydrostatic vertical adjustment of the top boundary height using (4) still produces a pressure along the top boundary that closely follows the specified constant value.

4 Summary

As discussed above, for deep atmosphere model applications it is important to allow the simulation domain to expand and contract vertically in response to diabatic heating and cooling. To permit this behavior in models employing a height based vertical coordinate, KS22 proposed a coordinate transform that replaces the rigid-lid upper boundary with one that follows a constant pressure material surface, and demonstrated its viability in a 2-D idealized diurnal heating test case. Here, we have extended the testing of this boundary formulation to global applications, including the simulation of real data cases using full physics model configurations.

Extending the idealized diurnal heating case tested in KS22 to a global implementation confirmed that the simulation maintained good stability and qualitative similarity to the behavior seen in a representative WACCM-X simulation. In the absence of realistic model physics we found that to maintain a nearly steady periodic diurnal cycle, it is necessary to include a Rayleigh damping term in the thermodynamic equation as a surrogate for Newtonian cooling that acts as a radiative damping mechanism. As demonstrated in KS22, for this thermospheric application, a floating upper boundary surface is essential to avoid large amplitude artificial thermal perturbations forming in the vicinity of the upper boundary.

For the real data test cases, we restricted our testing to simulations with the top boundary at a nominal height of $H_0 = 70$ km in order to initialize MPAS-A within the range of data contained within the ERA5 analyses. With a nominal horizontal mesh spacing of 120 km, we conducted extended (30 day) simulations in each of the four seasons to verify that the numerical integrations were stable and the results were well behaved. To ensure stability, we reduced the value of the extrapolation coefficient in (4) to $\alpha = 0.2$, which still allowed the top boundary to closely follow a specified constant pressure surface. In

https://doi.org/10.5194/egusphere-2026-3568
Preprint. Discussion started: 28 July 2026

comparing the simulations at 10 days, we documented good qualitative agreement with the corresponding ERA5 analyses, although the height variations in the top boundary surface were noticeably larger in the MPAS-A simulations than in the ERA5 analyses.

In comparing the real-data MPAS-A simulations with the constant pressure top boundary to those conducted with a rigid lid, we found good overall agreement, as illustrated in Fig. 5. This suggests that differences between the MPAS-A simulations and the ERA5 analyses are not the result of issues with the top boundary formulation. It also indicates that for applications with a model top in the vicinity of 70 km, either a constant pressure upper boundary or a rigid lid may be suitable, as suggested by Pu and Kalnay (2018).

Finally, we documented that the constant pressure upper boundary formulation remains viable at higher resolutions, with simulations on a 15 km mesh and on a 60-3 km variable resolution mesh. Focusing on a region above the Southern Andes mountains in South America, we have shown that the variations in the top boundary height are well resolved and deviations from the target constant pressure remain small, even with the presence of significant gravity wave activity due to the strong south polar jet.

MPAS-A is currently being integrated into the new version of CESM as a dynamical core for CAM-SIMA. Building on that, we plan to further develop MPAS-A as a nonhydrostatic dynamical core for WACCM and WACCM-X, which will include the new constant pressure upper boundary formulation described in this paper that will be suitable for deep atmosphere applications. In adapting MPAS-A into WACCM and WACCM-X, we intend to utilize the high altitude atmospheric physics within those models, which should further improve our capabilities in deep atmosphere model applications.

Code and data availability. The MPAS-A model code is publicly available, and version v8.3.1 can be found in the Zenodo repository: https://zenodo.org/record/15686368. The ERA5 reanalysis data is publically available from the Copernicus Climate Change Service (C3S) Climate Data Store (CDS),DOI: 10.24381/cds.143582cf (Hersbach et al., 2017) and can be downloaded from https://cds.climate.copernicus.eu/datasets/reanalysis-era5-complete?tab=d_download.

Author contributions. All authors contributed to the design of the numerical simulations and analysis of the results. JK led writing of the manuscript and prepared the figures. All authors contributed to revisions of the text.

Competing interests. The contact author has declared that none of the authors has any competing interests.

Acknowledgements. This material is based upon work supported by the NSF National Center for Atmospheric Research, which is a major facility sponsored by the National Science Foundation under Cooperative Agreement No. 1755088.

https://doi.org/10.5194/egusphere-2026-3568
Preprint. Discussion started: 28 July 2026

References

Borchert, S., Zhou, G., Baldauf, M., Schmidt, H., Zängl, G., and Reinert, D.: The upper-atmosphere extension of the ICON general circulation model (version: ua-icon-1.0), Geosci. Model Dev., 12, 3541–3569, 2019.

Dickinson, R. E., Ridley, E. C., and Roble, R. G.: A three-dimensional general circulation model of the thermosphere, Journal of Geophysical Research: Space Physics, 86, 1499–1512, https://doi.org/10.1029/JA086iA03p01499, 1981.

Griffith, M. J., Jackson, D. R., Griffin, D. J., and Budd, C. J.: Stable extension of the unified model into the mesosphere and lower thermosphere, J. Space Weather Space Clim., 10, 1–20, https://doi.org/10.1051/swsc/2020018, 2020.

Hersbach, H., Bell, B., Berrisford, P., Hirahara, S., Horányi, A., Muñoz-Sabater, J., Nicolas, J., Peubey, C., Radu, R., Schepers, D., Simmons, A., Soci, C., Abdalla, S., Abellan, X., Balsamo, G., Bechtold, P., Biavati, G., Bidlot, J., Bonavita, M., DeChiara, G., Dahlgren, P., Dee, D., Diamantakis, M., Dragani, R., Flemming, J., Forbes, R., Fuentes, M., Geer, A., Haimberger, L., Healy, S., Hogan, R., Hólm, E., Janisková, M., Keeley, S., Laloyaux, P., Lopez, P., Lupu, C., Radnoti, G., de Rosnay, P., Rozum, I., Vamborg, F., Villaume, S., and Thépaut, J.-N.: Complete ERA5 from 1940: Fifth generation of ECMWF atmospheric reanalyses of the global climate, Copernicus Climate Change Service (C3S) Data Store (CDS), https://doi.org/DOI: 10.24381/cds.143582cf, 2017.

Hersbach, H., Bell, B., and Berrisford, P.: The ERA5 global reanalysis, Q. J. R. Meteorol. Soc., 146, 1999–2049, https://doi.org/10.1002/qj.3803, 2020.

Kamalli, S., Liu, H.-L., Skamarock, W., Klemp, J. B., Vitt, F., and Lauitzen, P. H.: Development of WACCM with the non-hydrostatic MPAS-A dynamical core., J. Adv. Model. Earth Syst., 16, e2023MS004 108, https://doi.org/10.1029/2023MS004108, 2024.

Kelly, J. F., Reddy, S., Giraldo, F. X., Reinecke, P. A., Emmert, J. T., Jones, M., and Eckermann, S. D.: A physics-based open atmosphere boundary condition for height-coordinate atmospheric models, J. Comput. Phys., 482, 112 044, https://doi.org/10.1016/j.jcp.2023.112044, 2023.

Klemp, J. B.: A terrain following coordinate with smoothed coordinate surfaces, Mon. Wea. Rev., 139, 2163–2169, doi:10.1175/MWR–D–10–05 046.1, 2011.

Klemp, J. B. and Skamarock, W. C.: Adapting the MPAS dynamical core for applications extending into the thermosphere, J. Adv. Model. Earth Syst., 13, https://doi.org/10.1029/2021MS002499, 2021.

Klemp, J. B. and Skamarock, W. C.: A constant pressure upper boundary formulation for models employing height-based vertical coordinates, Mon. Wea. Rev., 150, 2175–2186, https://doi.org/10.1175/MWR-D-21-0328.1, 2022, hereafter KS22.

Liu, H.-L., Foster, B. T., Hagan, M. E., McInerney, J. M., Maute, A., Qian, L., Richmond, A. D., Roble, R. G., Solomon, S. C., Garcia, R. R., Kinnison, D., Marsh, D. R., Smith, A. K., Richter, J., Sassi, F., and Oberheide, J.: Thermosphere extension of the Whole Atmosphere Community Climate Model, Journal of Geophysical Research: Space Physics, 115, https://doi.org/10.1029/2010JA015586, 2010.

Liu, H.-L., Bardeen, C. G., Foster, B. T., Lauritzen, P., Liu, J., Lu, G., Marsh, D. R., Maute, A., McInerney, J. M., Pedatella, N. M., Qian, L., Richmond, A. D., Roble, R. G., Solomon, S. C., Vitt, F. M., and Wang, W.: Development and validation of the Whole Atmosphere Community Climate Model with Thermosphere and Ionosphere Extension (WACCM-X 2.0), J. Adv. Model. Earth Syst., 10, 381–402, https://doi.org/10.1002/2017MS001232, 2018.

Müller, W. A., Lorenz, S., Pham, T. V., Schneidereit, A., Brokopf, R., Brovkin, V., Brüggemann, N., Chegini, F., Dommenget, D., Fröhlich, K., Früh, B., Gayler, V., Haak, H., Hagemann, S., Hanke, M., Ilyina, T., Jungclaus, J., Köhler, M., Korn, P., Kornblueh, L., Kroll, C. A., Krüger, J., Castro-Morales, K., Niemeier, U., Pohlmann, H., Polkova, I., Potthast, R., Riddick, T., Schlund, M., Stacke, T., Wirth, R., Yu,

https://doi.org/10.5194/egusphere-2026-3568
Preprint. Discussion started: 28 July 2026

D., and Marotzke, J.: The ICON-based Earth System Model for climate predictions and projections (ICON XPP v1.0), Geosci. Model Dev., 18, 9385–9415, https://doi.org/10.5194/gmd-18-9385-2025, 2025.

Pu, Z. and Kalnay, E.: Numerical Weather Prediction Basics: Models, Numerical Methods, and Data Assimilation. In: Duan Q., Pappenberger F., Thielen J., Wood A., Cloke H., Schaake J. (eds), Handbook of Hydrometeorological Ensemble Forecasting, Springer, Berlin, Heidelberg, 2018.

Ridley, A., Deng, Y., and Tóth, G.: The global ionosphere-thermosphere model, Journal of Atmospheric and Solar-Terrestrial Physics, 68, 839 – 864, https://doi.org/10.1016/j.jastp.2006.01.008, 2006.

Skamarock, W. C., Klemp, J. B., Duda, M. G., Fowler, L. D., Park, S.-H., and Ringler, T.: A multiscale nonhydrostatic atmospheric model using centroidal Voronoi tesselations and C-grid staggering, Mon. Wea. Rev., 140, 3090–3105, https://doi.org/10.1175/MWR-D-11-00215.1, 2012.

Skamarock, W. C., Klemp, J. B., Dudhia, J., Gill, D. O., Liu, Z., Berner, J., Wang, W., Powers, J. G., Duda, M. G., Barker, D. M., and Huang, X.-Y.: A Description of the Advanced Research WRF Version 4, NCAR Technical Note NCAR/TN-556+STR, https://doi.org/10.5065/1dfh-6p97, 2019.

Willett, M., Brooks, M., Bushell, A., Earnshaw, P., Smith, S., Tomassini, L., Best, M., Boutle, I., Brooke, J., Edwards, J. M., Elvidge, A. D., Furtado, K., Hardacre, C., Hartley, A. J., Hewitt, A. J., Johnson, B., Lock, A., Malcolm, A., Mulcahy, J., Müller, E., Renfrew, I. A., Rumbold, H., Rooney, G. G., Sellar, A., Ujiie, M., van Niekerk, A., Wiltshire, A., and Whitall, M.: The Met Office Unified Model Global Atmosphere 8.0 and JULES Global Land 9.0 configurations, Geosci. Model Dev., 19, 1473–1517, https://doi.org/10.5194/gmd-19-1473-2026, 2026.